Study on Magnetic Shielding for Performance Improvement of Axial-Field Dual-Rotor Segmented Switched Reluctance Machine

Wei Sun, *Student Member, IEEE*, Qiang Li, Le Sun, *Member, IEEE*, and Xuefeng Jiang, *Member, IEEE*

***Abstract*—A category of permanent-magnet-shield (PM-shield) axial-field dual-rotor segmented switched reluctance machines (ADS-SRMs) are presented in this paper. These topologies are featured by using the magnetic material to shield the flux leakage in the stator and rotor parts. Besides, the deployed magnets weaken the magnetic saturation in the iron core, thus increasing the main flux. Hence, the torque-production capability can be increased effectively. All the PM-shield topologies are proposed and designed based on the magnetic equivalent circuit (MEC) model of ADS-SRM, which is the original design deploying no magnet. The features of all the PM-shield topologies are compared with the original design in terms of the magnetic field distributions, flux linkages, phase inductances, torque components, and followed by their motion-coupled analyses on the torque-production capabilities, copper losses, and efficiencies. Considering the cost reduction and the stable ferrite-magnet supply, an alternative proposal using the ferrite magnets is applied to the magnetic shielding. The magnet demagnetization analysis incorporated with the thermal behavior is performed for further verification of the motor performance.**

***Index Terms*—Switched reluctance machine (SRM), magnetic shielding, magnetic equivalent circuit (MEC), demagnetization, thermal behavior.**

I. INTRODUCTION

SWITCHED reluctance machine (SRM) is becoming research focus in recent years due to its unique advantages such as simple and rugged construction, low cost, fault-tolerant operation capability, and high-speed and high-temperature operation adaptabilities [1]-[3]. These features enable SRM a good candidate for electric vehicles, electric bicycle, aircraft, railway transport, and other transportation appliances [4]-[9].

In spite of the above described advantages, some issues still exist for SRM, which are the challenges for the further applications of SRM. The first is the lower torque density compared with the permanent-magnet synchronous motor (PMSM), which means that higher current density is necessary for the same energy conversion [10]. This is caused by the absence of the high-energy-density permanent magnet (PM) in the magnetic structure. To improve the torque density, many investigations have been implemented on the modified motor topologies such as the axial-field topologies, the dual-stator/rotor configurations, the optimal stator/rotor pole combinations, etc. [11]-[13]. Besides, a group of SRM featured with the segmental stator or rotor is introduced for the torque-density improvement [2], [14].

Although the torque density can be effectively improved through the above methods, the issue concerned with the fringing and leakage field is remarkable in SRM due to double saliency, which is inherent in SRM. It has been recognized that some of the fringing field can generate the braking torque [15]. The leakage field does not contribute to any torque production and can reduce the utilization of the magnetomotive force (MMF) [16]. Besides, the leakage inductance increases the time constant of the phase winding, which will decrease the phase current and narrow the speed range [16]. Several methods have been proposed to reduce the fringing and leakage field in SRM, including the modification of the winding layouts, the utilization of the grain-oriented steel sheet, the optimization of the stator/rotor pole profile, and the PM shield [15], [17]-[20]. However, the possibilities for the ferrite magnets in the PM-shield configuration have never been considered, and the demagnetization of the magnetic material has never been analyzed.

This paper presents a category of PM-shield axial-field dual-rotor segmented switched reluctance machine (ADS-SRM) by deploying the magnets to shield the flux leakage and improve the torque output. First, the flux leakage in ADS-SRM is revealed, and the possible PM-shield configurations for the leakage field shielding are introduced based on the magnetic equivalent circuit (MEC) models. Besides, the derivation of the adopted rare-earth magnet dimensions is delivered based on the MEC models. Second, the features of the rare-earth PM-Shield topologies are compared with the original design, which is the topology deploying no magnet, by three-dimensional (3D) finite-element method (FEM). As an extension, the possibilities for the ferrite magnets are analyzed, and the comparative study between the rare-earth and ferrite PM-shield configurations is performed. Finally, the magnet demagnetization analysis on the

Manuscript received July 17, 2020; revised November 29, 2020; accepted January 05, 2021. date of publication March 25, 2021; date of current version March 18, 2021.

This work was supported in part by the National Natural Science Foundation of China under Grant 51807094. *(Corresponding author: Wei Sun)*

The authors are with the School of Automation, Nanjing University of Science and Technology, Nanjing 210094, China (e-mails: sunwei_njust@foxmail.com; chnliqiang@njust.edu.cn; sunle@njust.edu.cn; jxf@njust.edu.cn).

Digital Object Identifier 10.30941/CESTEMS.2021.00007

rare-earth and ferrite PM-shield ADS-SRMs is implemented through 3D FEM and the lumped-parameter thermal network (LPTN) models.

II. Introduction of PM-Shield ADS-SRM

A. Introduction to ADS-SRM

The 3D view of ADS-SRM is shown in Fig. 1 [21]. As shown in Fig. 1(a), the machine consists of a single internal stator and two external rotors. As shown in Fig. 1(b), epoxy potting under the vacuum condition is applied to the phase windings, and therefore, all the stator parts are assembled robustly. Besides, all eight rotor segments at each side are inserted in a nonmagnetic rotor bracket. Fig. 1(c) shows the prototype of ADS-SRM. The specifications and main geometric parameters are given in Table I. The flux density distributions at the phase excitation of 8A near typical rotor positions, i.e. unaligned and aligned rotor positions, are shown in Figs. 2(a) and 2(b), respectively. It is found that the leakage field is significant near unaligned rotor position, especially between the excitation pole and the flux-conductive rings.

For better reflection of the flux leakage, 2D FEM is carried out on the 2D analysis model plot in Fig. 3. The 2D analysis model can reflect the performance of ADS-SRM very well as the comparison of the static-torque characteristics shown in Fig. 4. The flux line distributions in the 2D analysis model at unaligned and aligned rotor positions along with the corresponding MEC models are shown in Fig. 5. The red flux paths in Fig. 5(c) represent the leakage flux paths between the excitation pole and the flux-conductive ring. The leakage flux linked by the coil itself and the leakage flux at aligned rotor position, as shown in Fig. 5(b), are negligible due to the sparse leakage flux lines. In addition, it is observed from Figs. 5(a) and 5(c) that the leakage flux paths are normal to the rotor moving direction. The leakage flux paths bypass a portion of magnetic flux in the air gap, thus reducing the electrical utilization and narrowing the speed range [16].

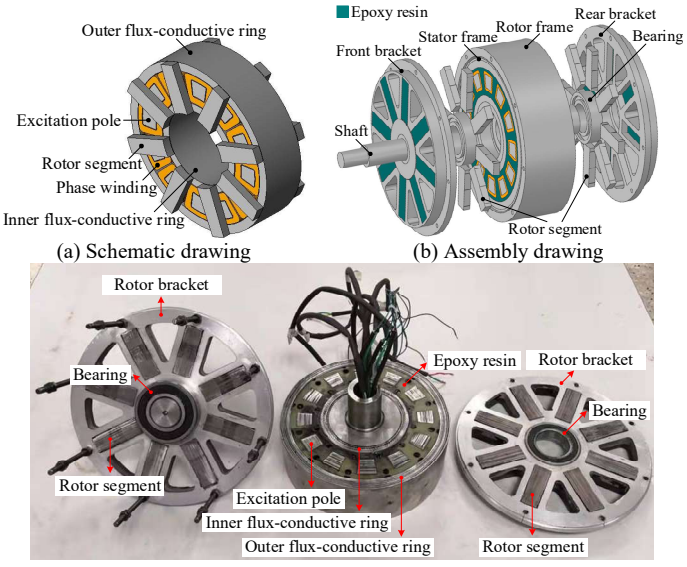

(a) Schematic drawing (b) Assembly drawing

(c) Prototype of ADS-SRM.

Fig. 1. 3D view of ADS-SRM.

TABLE I
MAIN SPECIFICATIONS AND GEOMETRIC PARAMETERS

Parameters	Values
Stator/rotor pole number	12/8
Phase number	3
Rated power (kW)	1
Base speed (r/min)	2000
Outer diameter (mm)	200
Inner diameter (mm)	87.3
Mean armature diameter (mm)	145.2
Stator axial length (mm)	50.8
Air-gap length (mm)	0.5
Phase turn number	225×4
Grade	50DW470

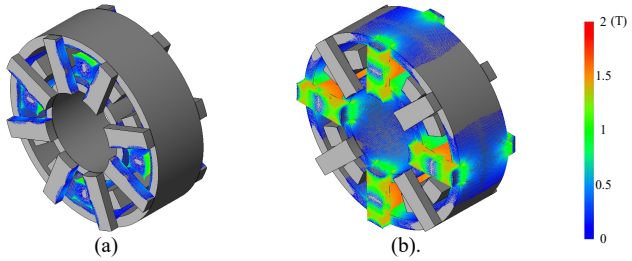

(a) (b).

Fig. 2. Flux density distributions at (a) unaligned and (b) aligned rotor positions.

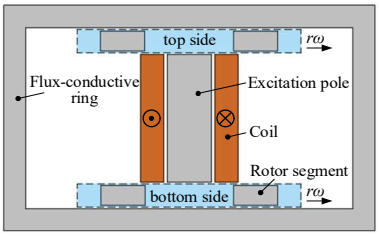

Fig. 3. 2D analysis model of ADS-SRM.

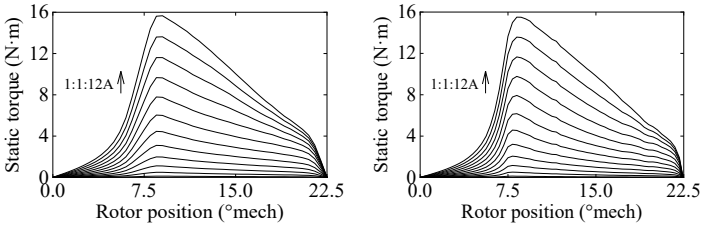

Fig. 4. Static-torque characteristics of (a) ADS-SRM and (b) 2D analysis model.

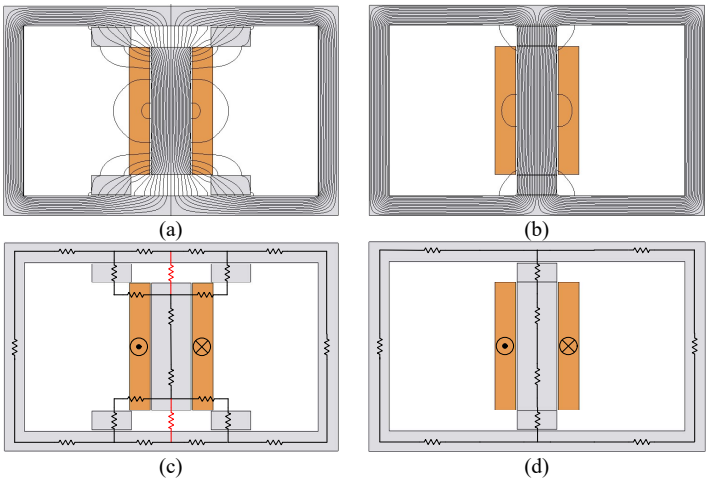

Fig. 5. Flux line distributions in the 2D analysis model at (a) unaligned and (b) aligned rotor positions, and the corresponding MEC models at (c) unaligned and (d) aligned rotor positions.

B. Inspiration for Leakage Field Reduction

In the previous section, the leakage field in ADS-SRM is reflected by the 2D analysis model. However, the leakage field in ADS-SRM should be much more complex due to the multiple air gaps, but it has no impact on the discussion on the solutions.

To shield the flux leakage in Fig. 5(a), the additional MMF in reverse series in the gap between the excitation pole and the flux-conductive ring is necessary, as shown in Fig. 6(a). It is observed that the PMs are installed with the magnetic polarity conflicting with that of the excitation pole. The corresponding flux line distributions are shown in Fig. 6(b). It is indicated in Fig. 6(b) that the leakage flux is almost eliminated. By contrast, much more flux lines go through the rotor segments. The comparison of the static-torque characteristics between the 2D analysis model without and with the PM shield at the phase excitation of 8A is shown in Fig. 7. It can be observed that, with the PM shield, the torque-production capability increases significantly. Hence, 2D finite-element analysis (FEA) proves the effectiveness of the PM shield for the leakage field shielding and the torque out improvement.

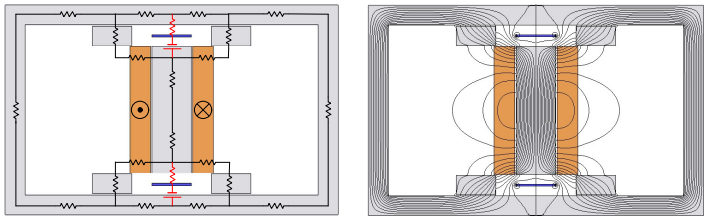

(a) (b)

Fig. 6. Topology modification of the 2D analysis model of ADS-SRM. (a) Modified MEC model. (b) Flux line distributions after modification.

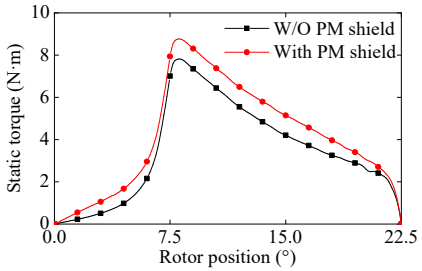

Fig. 7. Comparison of the static-torque characteristics without and with PM shield based on the 2D analysis model.

C. MEC Models of ADS-SRM

For further discussion on the PM-shield application in the 3D model, it is necessary to sketch the flux patterns of ADS-SRM. As stated in the foregoing section, the flux leakage is much more significant near unaligned rotor position. In this paper, the emphasis is laid on the leakage field suppression at this position. The flux patterns at unaligned rotor position is shown in Fig. 8. The corresponding MEC model is shown in Fig. 9. In Fig. 9, F_1 represents the MMF provided by the coils, R_x is the reluctance in each branch. The red flux paths in Fig. 9 denote the leakage flux paths. It is indicated that the MEC model of the 3D model is much more complex than that in Fig. 5. The leakage field exists in two ways. One is between the side surfaces of the excitation pole and the flux-conductive rings, and the other between their end surfaces. Hence, the solutions for the leakage field reduction in the 3D model are revealed, which will be introduced in detail next.

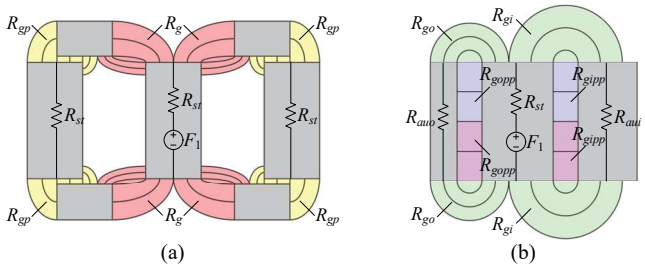

(a) (b)

Fig. 8. Flux patterns in the air region at unaligned rotor position. (a) Flux patterns in the circumferential cross section. (b) Flux patterns in the radial cross section of the excitation pole.

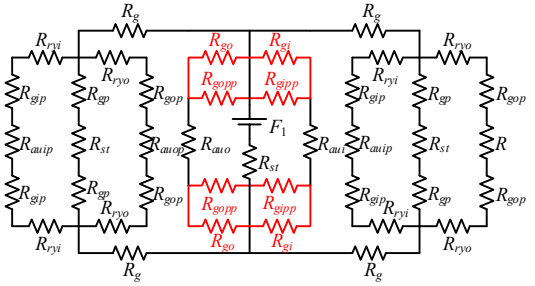

Fig. 9. MEC model of ADS-SRM at unaligned rotor position.

D. Configurations of PM-Shield ADS-SRM

As shown in Figs. 8 and 9, the two existence ways for the flux leakage are at the stator and rotor sides, respectively. When the PMs are installed at both the stator and rotor sides for the flux leakage shielding, there are two possible configurations (Schemes #1 and #2) can meet the requirement, which are shown in Fig. 10. And the corresponding motor geometries are shown in Fig. 11. In Fig. 10, F_{PM1} and F_{PM2} represent the MMFs provided by the PMs installed at the front and back sides of the excitation pole, respectively. F_{PM3} and F_{PM4} in Fig. 10(a) represent the MMFs provided by the PMs installed at the front and back sides of the excitation-pole end surfaces, respectively. F_{PM3} in Fig. 10(b) refers to the PMs installed facing the excitation-pole end surfaces.

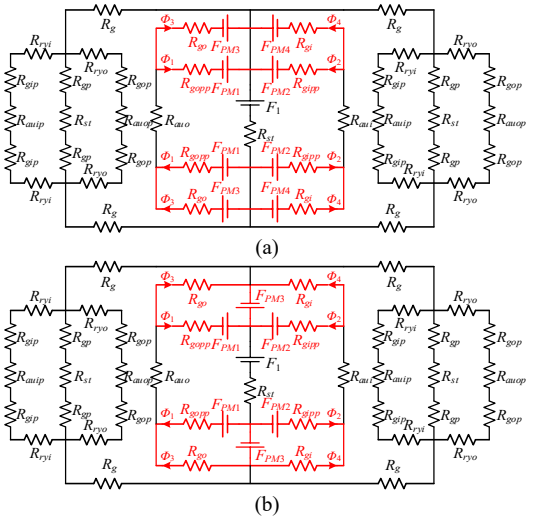

(a)

(b)

Fig. 10. Modified MEC models for the PM-shield ADS-SRM in Schemes (a) #1 and (b) #2.

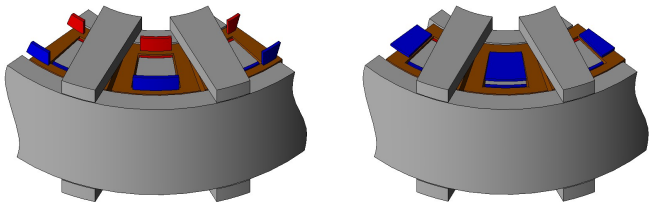

(a) (b)

Fig. 11. PM-shield ADS-SRM in Schemes (a) #1 and (b) #2.

E. Dimension Design of the PMs

For the flux leakage shielding in ADS-SRM, the installed PMs should overlap the cross sections of the leakage flux paths. Referring to the two proposals of the PM-shield ADS-SRMs in the foregoing section, the PMs are in the two geometric shapes shown in Fig. 12. One is in the arcuate shape and the other in the planar shape. In Fig. 12, d_{PMx} and h_{PMx} are the magnet thickness and height, respectively, and are derived based on the MEC models.

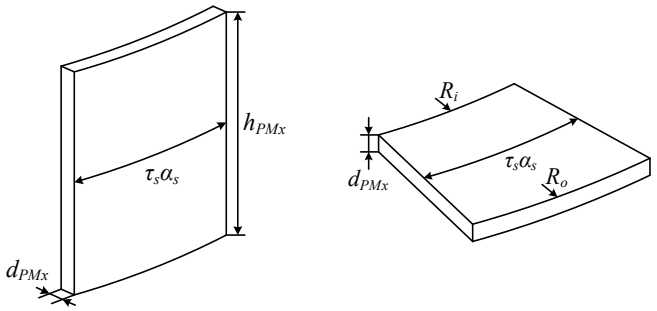

(a) (b)

Fig. 12. Magnet geometry in the (a) arcuate and (b) planar shapes.

Near unaligned rotor position, the iron-core saturation can be neglected. Thus, only the air-gap reluctances are taken into account. According to the Kirchhoff's laws based on the MEC model of each scheme, the mesh equations of the MEC models can be obtained and are in the form of (1). In (1), $[R]$ and $[\Phi]$ are the matrix of reluctances in each branch and the matrix of magnetic flux in each loop, respectively, and $[U]$ is the matrix of MMF sources.

$$[R][\Phi]=[U] \tag{1}$$

By solving (1), the magnetic flux Φ_x flowing in the leakage flux path can be obtained as (2), where R_x is the reluctance cascaded with F_{PMx}. The thickness d_{PMx} of the magnet for the flux leakage shielding, i.e. Φ_x=0 Wb, can be obtained as (3).

$$\Phi_x=\frac{2F_{PMx}-F_1}{2R_x} \tag{2}$$

$$d_{PMx}=\frac{F_1}{2H_c} \tag{3}$$

In this design, for either the arcuate- or planar-shape magnet, the thicknesses are 1 mm as the coercive force (H_c) of the employed rare-earth magnet (Nd-Fe-B) is about 900 kA/m at the magnet temperature of 60°C. The MMF of the coils wrapped around each excitation pole (F_1) is 8×225 A·T.

Besides, the cross section of the planar-shape magnet at the rotor side coincides with that of the excitation pole, and the height h_{PMx} of the arcuate-shape magnet depends on the motor side, i.e. the stator side or the rotor side. For the arcuate-shape magnets at the stator side, h_{PMx} equals half of the axial stator length, while that at the rotor side in Scheme #1 is determined after optimization. Fig. 13 shows the influence of the height of the arcuate-shape magnets at the rotor side on the flux linkage at unaligned and aligned rotor positions in Scheme #1. It is observed that h_{PMx} can have much more significant effect on the flux linkage at unaligned rotor position. To have a fair comparison of the two PM-shield schemes (#1 and #2), their magnet volumes should be identical. Hence, h_{PMx} of the arcuate magnet at the rotor side in Scheme #1 equals 9.75 mm. The total magnet volumes for both schemes are 29 cm^3. The magnet volume at the stator side is in majority, which is 23.1 cm^3.

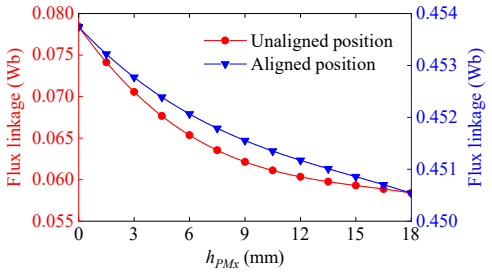

Fig. 13. Influence of h_{PMx} on the flux linkage at unaligned and aligned rotor positions in Scheme #1 at the phase excitation of 8A.

III. Features of Rare-Earth PM-Shield ADS-SRMs

A. Magnetic Field Distributions

The magnetic field distributions in the original design, i.e. the magnet-free topology, and the two PM-shield schemes at unaligned rotor position at the phase excitation of 8A are presented in Fig. 14. The red and white arrows in Fig. 14 indicate the current flow and magnetic field directions, respectively. It is observed that the PMs can effectively modulate the magnetic field around the current exciting pole, and the leakage field is effectively reduced. Besides, it is noted that no-load magnetic field exists in the PM-shield configurations.

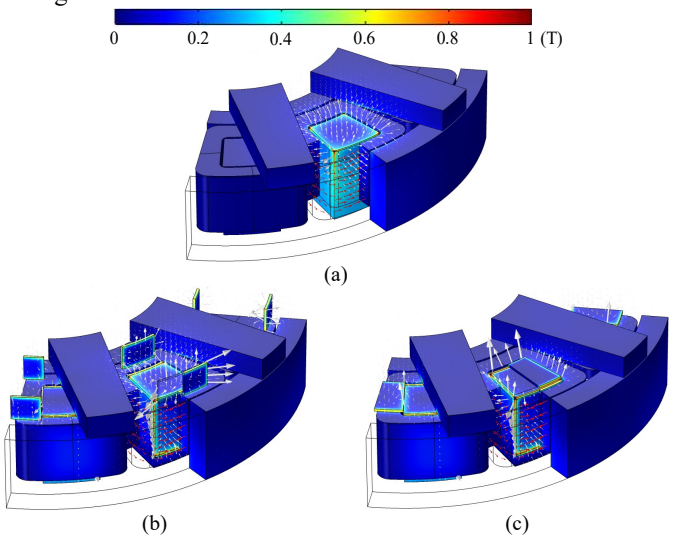

(a)

(b) (c)

Fig. 14. Magnetic field distributions in (a) original design, (b) Scheme #1, and (c) Scheme #2.

B. Flux-Linkage Characteristics

Due to the magnetic saturation in the iron core, the flux-linkage loci with the increasing phase current levels are in nonlinearity. Unlike the original design, the total flux linkage of the PM-shield ADS-SRM consists of three components, i.e. the self-flux linkage, the mutual flux linkage, and the PM flux linkage. The frozen permeability technique is adopted to obtain these three components [22], [23].

Figs. 15(a) and 15(b) give the self- and mutual flux linkages, respectively. As shown in 15(a), the maximum self-flux linkage is achieved at aligned rotor position, and the minimum at unaligned rotor position. It is found that the PM shield increases the self-flux linkage at aligned rotor position since the PMs weaken the magnetic saturation in the iron core at high current levels, while the self-flux linkages are almost the same near unaligned rotor position. As the area enclosed by the self-flux linkage loci at the unaligned and aligned rotor positions denotes the amount of energy conversion, the torque-production capabilities of the PM-shield ADS-SRMs are apparently higher than that of the original design.

In addition, the PMs have significant influence on the mutual flux linkages at aligned rotor position as shown in Fig. 15(b) at high current levels. The area enclosed by the unaligned and aligned mutual flux linkage loci of the PM-shield schemes is significantly smaller than that of the original design. This effect will be detailed in the following sections.

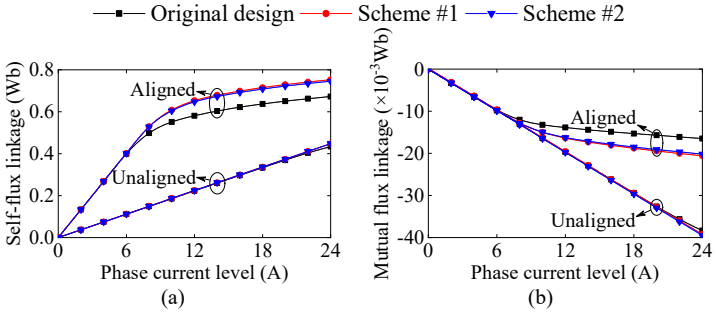

Fig. 15. Comparisons of (a) the self-flux linkage diagrams and (b) the mutual flux linkage diagrams.

According to the voltage equation (4) of the PM-shield ADS-SRM, the contribution of the PM flux linkage to the torque production can be evaluated by the derivatives of the PM flux linkage with respect to the rotor position as shown in Fig. 16. The unsmoothed curves in Fig. 16 may be due to the error of finite-element computation since the accuracy of the simulation results is closely related to the mesh densities of the finite-element models. It is observed that, in the positive-torque zone, i.e. 0-22.5°mech, the amplitude of $\mathrm{d}\Psi_{PM}/\mathrm{d}\theta$ in Scheme #2 is much higher than that in Scheme #1. Hence, Scheme #2 is able to produce higher toque. This will also be detailed in the following sections.

$$V_{DC} = ir_s + \Omega \frac{\mathrm{d}\left(\Psi_{self} + \Psi_{mutual} + \Psi_{PM}\right)}{\mathrm{d}\theta} \tag{4}$$

where V_{DC}, i, r_s, and Ω are the DC-link voltage, instantaneous phase current, phase resistance, and rotor speed, respectively. Ψ_{self}, Ψ_{mutual}, and Ψ_{PM} are the self-flux linkage, mutual flux linkage, and PM flux linkage, respectively.

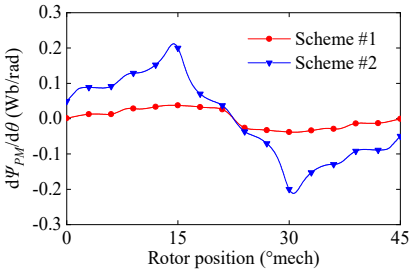

Fig. 16. Comparison of the derivatives of the PM flux linkages with respect to the rotor position in the PM-shield schemes.

C. Self- and Mutual Inductances

In order to evaluate the contributions of the self- and mutual flux linkages to the resultant torques, the self- and mutual inductances are analyzed. Based on the frozen permeability technique, the self-inductance (L_A) and mutual inductance (M_{AB}) at different current levels (1A, 8A, and 16A) are obtained as shown in Fig. 17. The self- and mutual inductances of other phases can be obtained by (5) and (6), respectively.

$$L_A(\theta) = L_B(\theta + 15°) = L_C(\theta + 30°) \tag{5}$$

$$M_{AB}(\theta) = M_{BC}(\theta + 15°) = M_{CA}(\theta + 30°) \tag{6}$$

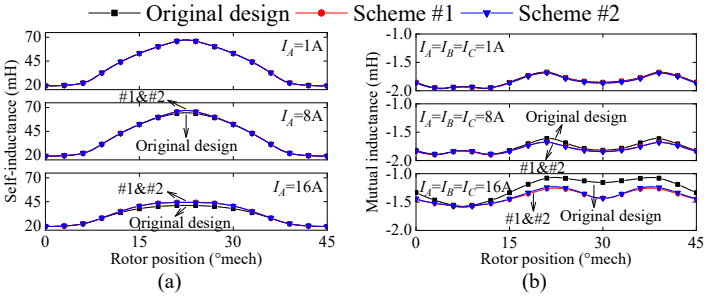

Fig. 17. Comparison of (a) the self-inductance L_A and (b) the mutual inductance M_{AB} at different current levels (1A, 8A, and 16A).

It is indicated in (4) that the resultant torque in the PM-shield ADS-SRM consists of the reluctance torque and the PM torque. Like general SRMs, the reluctance torque is obtained by (7). It is indicated that the reluctance torque consists of two components, i.e. the self-reluctance torque and the mutual reluctance torque. The two components are proportional to the derivatives of the self- and mutual inductances, respectively. The derivatives of the self- and mutual inductances, i.e. $\mathrm{d}L_A/\mathrm{d}\theta$ and $\mathrm{d}M_{AB}/\mathrm{d}\theta$, in the original design and the two PM-shield schemes are shown in Fig. 18. It is observed that the values of both $\mathrm{d}L_A/\mathrm{d}\theta$ and $\mathrm{d}M_{AB}/\mathrm{d}\theta$ are individually identical for the original design and the PM-shield schemes at low current levels. However, when the current level becomes high enough, the values of $\mathrm{d}L_A/\mathrm{d}\theta$ of the PM-shield schemes will exceed that of the original design, leading to higher self-reluctance torques. Besides, it is apparent that the value of $\mathrm{d}M_{AB}/\mathrm{d}\theta$ is small enough compared with that of $\mathrm{d}L_A/\mathrm{d}\theta$, resulting in ignorable mutual reluctance torque component.

$$\begin{aligned} T = {} & \frac{1}{2} i_A^2 \frac{\mathrm{d}L_A}{\mathrm{d}\theta} + \frac{1}{2} i_B^2 \frac{\mathrm{d}L_B}{\mathrm{d}\theta} + i_C^2 \frac{\mathrm{d}L_C}{\mathrm{d}\theta} \\ & + i_A i_B \frac{\mathrm{d}M_{AB}}{\mathrm{d}\theta} + i_B i_C \frac{\mathrm{d}M_{BC}}{\mathrm{d}\theta} + i_C i_A \frac{\mathrm{d}M_{CA}}{\mathrm{d}\theta} \end{aligned} \tag{7}$$

where i_A, i_B, and i_C are three phase instantaneous currents.

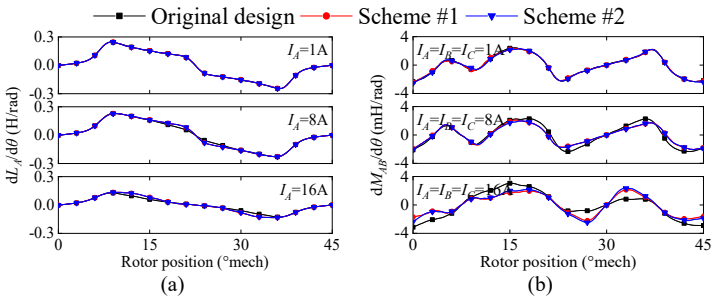

Fig. 18. Comparison of the derivatives of (a) the self-inductance L_A and (b) the mutual inductance M_{AB} with respect to the rotor position at different current levels.

D. Torque-Component Analysis

Fig. 19 shows the static-torque characteristics of the original design and the PM-shield schemes at the current levels of 8A and 16A. It proves the advantage of the PM installation for the significantly improved torque output. To evaluate the contribution of the PMs to the torque generations, the reluctance torque and the PM torque are obtained by the frozen permeability technique, and the results are shown in Figs. 20 and 21, respectively. For further insight into the effect of the PMs on the torque qualities, the detent torques in the two schemes are computed by 3D FEM under the no-load condition. Fig. 22 shows their detent torques.

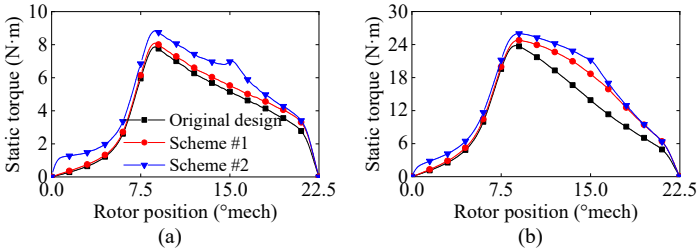

Fig. 19. Static-torque characteristics of the original design and the two PM-shield schemes at the current level of (a) 8A and (b) 16A.

1) Reluctance torque: As shown in Fig. 20, the reluctance torques in all configurations are almost identical at low current levels. However, at high current levels, the reluctance torque increases significantly in the PM-shield schemes.

2) PM torque: The PM torques contribute to the torque productions as shown in Fig. 21, and the PM torque in Scheme #2 is much higher than that in Scheme #1.

3) Detent torque: As shown in Fig. 22, the periods of the detent torques are 15°mech, and the detent torque in Scheme #2 is much more significant than that in Scheme #1. However, their magnitudes are far lower than the other torque components.

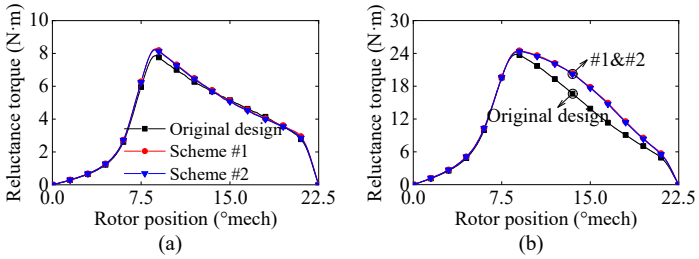

Fig. 20. Comparison of the reluctance-torque components at the current level of (a) 8A and (b) 16A.

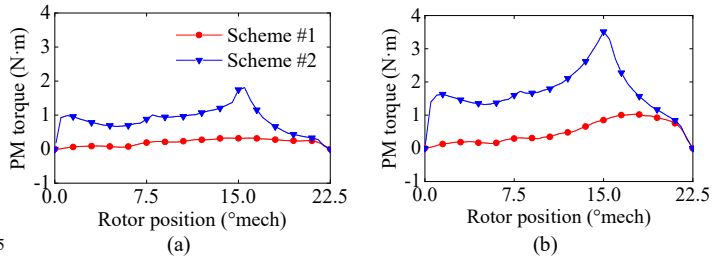

Fig. 21. Comparison of the PM-torque components at the current level of (a) 8A and (b) 16A.

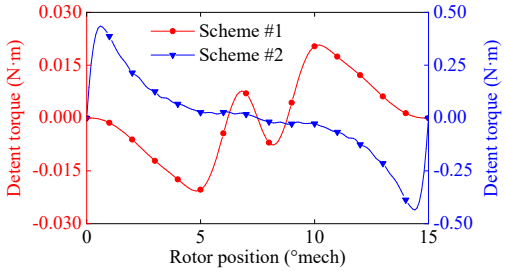

Fig. 22. Comparison of the detent torques in the PM-shield schemes.

E. Torque-Production Capabilities

At various current chopping levels from 0A to 24A, the average torque and torque ripple in all configurations are investigated, and the results are shown in Fig. 23. The torque ripple is calculated by (8), where T_{max}, T_{min}, and T_{avg} are the maximum, minimum, and average torques, respectively.

$$k_{ripple} = \frac{T_{\max} - T_{\min}}{T_{avg}} \tag{8}$$

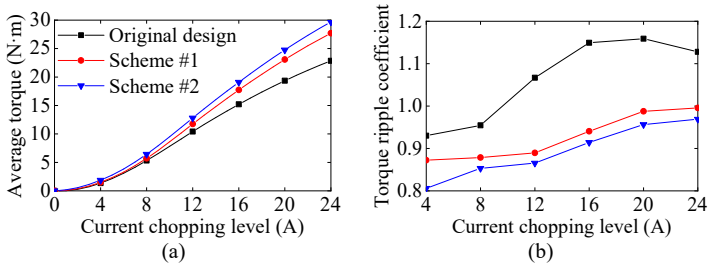

Fig. 23. Comparison of (a) the average torque and (b) the torque ripple coefficient in all configuration.

It is observed from Fig. 23 that through the introduction of the PM shield, the torque-production capabilities are greatly improved. In addition, Scheme #2 exhibits better performance for its higher average torque and lower torque ripple. With the current restraint of 8A, their mechanical characteristics are shown in Fig. 24. It further verifies the superiority of Scheme #2.

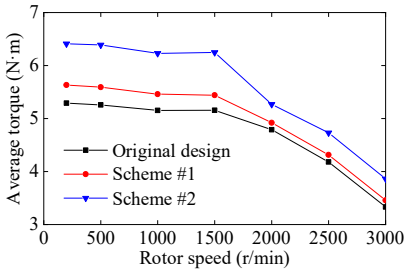

Fig. 24. Mechanical characteristics in all configurations.

F. Copper Loss

As the stator-installed PMs are mounted on the side surfaces of the excitation poles, the PM-shield configurations have longer coil length if the phase turn number and the iron-core dimensions keep constant. This leads to higher phase resistance. Besides, as shown in Fig. 17(a), the increased aligned self-inductances in the PM-shield configurations at higher current levels increase the time constants for the phase demagnetization. Moreover, as shown in (4) and Fig. 16, the back electromotive force (EMF) provided by the PMs suffers a portion of the DC-link voltage, reducing the voltage for the phase energizing. All these factors can affect the phase current waveforms.

The copper losses at the rated condition (1 kW at 2000 r/min) are shown in Table II, and Fig. 25 shows the variations of the average torque with the copper loss. It is found that, Scheme #2 produces the lowest copper loss at any average torque. Fig. 26 shows the variation of the average torque per unit copper loss with the increasing rotor speed at the current chopping level of 8A. It is indicated that Scheme #2 exhibits the best performance not only for its higher torque out, but also the lower copper loss.

TABLE II
COPPER LOSSES AT RATED CONDITION

Item	Original design	Scheme #1	Scheme #2
Copper loss (W)	160	159	143

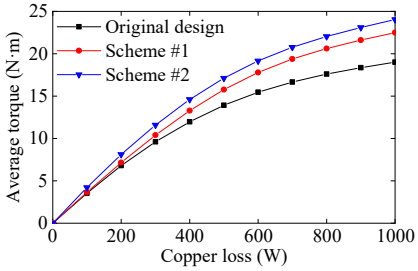

Fig. 25. Variations of the average torque with the copper loss.

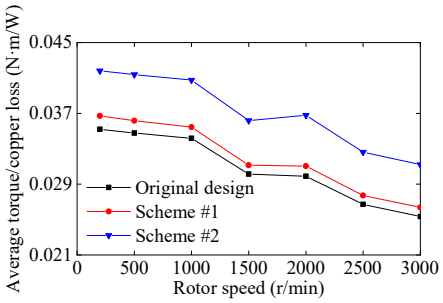

Fig. 26. Variation of the average torque per unit copper loss with the rotor speed at the current chopping level of 8A.

G. Efficiency

Based on the output power and the losses (including the copper loss, the magnet eddy-current loss, and the iron loss), the motor efficiencies can be computed. Fig. 27(a) shows the variation of efficiency at 500 r/min with the increasing current chopping level, and 27(b) shows the variation of efficiency at the constant current chopping level of 8A with the increasing rotor speed from 200 r/min to 3000 r/min. From Fig. 27, it is observed that the motor efficiencies in all configurations decrease monotonously with the increasing current chopping level, while they increase with the increasing rotor speed. Besides, Scheme #2 exhibits the highest efficiency.

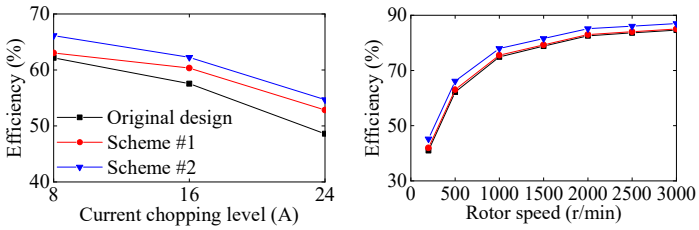

Fig. 27. Motor efficiencies in various configurations at (a) 500 r/min with the increasing current chopping levels and (b) the current chopping level of 8A with the increasing rotor speed.

IV. POSSIBILITIES FOR FERRITE PM-SHIELD ADS-SRM

The results from Section III suggest that the rare-earth PM shield can improve the motor performance significantly, and the PM-shield configuration in Scheme #2 stands out for its more superior performance than Scheme #1. In this section, an alternative proposal using the ferrite magnets is applied to the PM-shield configuration in Scheme #2. This is motivated by the cost reduction and the consideration of stable ferrite-magnet supply, although the ferrite magnets have the disadvantage of low energy density [24]. According to (3), to achieve the same effect as the rare-earth magnets, the thickness of the employed ferrite magnets (FB9B) should be 2.64 mm. The maximum slot-fill factor increases to 80%. The comparisons of the motor performances are shown in Figs. 28 and 29. It is indicated that the performance of the ferrite PM-shield ADS-SRM is comparable to the rare-earth configuration.

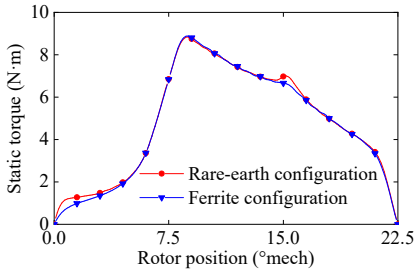

Fig. 28. Comparison of the static-torque characteristics between the rare-earth and ferrite PM-shield ADS-SRMs at the phase excitation of 8A.

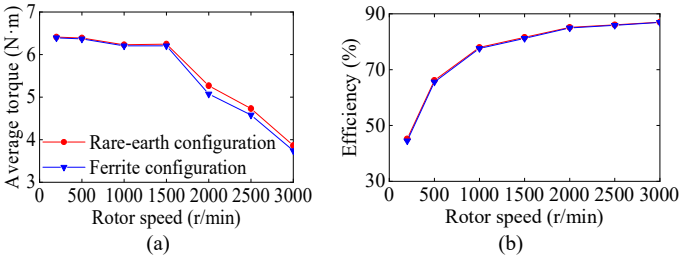

Fig. 29. Comparison of (a) the mechanical characteristics and (b) the efficiencies with the current restraint of 8A.

V. MAGNET DEMAGNETIZATION ANALYSIS

In previous sections, the rare-earth and ferrite PM-shield ADS-SRMs have been proved to have better torque-production

capabilities and higher efficiencies compared with the original design. However, the magnets are designed just for eliminating the leakage field, and the reluctance torque is still the dominant output way of the PM-shield configurations. Hence, in the normal operation, the flux densities in the magnets oscillate close to 0 T. This highlights the issue concerned with the magnet demagnetization as the motor's safe operation and overload capability depend on the magnets' demagnetization behavior. In this section, the magnet demagnetization analysis is performed on the rare-earth and ferrite PM-shield ADS-SRMs.

A. Magnet's Operating Point

To prevent working with loads exceeding the magnet's demagnetization limits, the magnet's operating points at several load conditions should be analyzed. The magnet's demagnetization limits are highly related with the magnet temperature and will be discussed in detail in the next section. The flux-density distributions over the magnet span at full load at various rotor positions are shown in Fig. 30, and those at unaligned rotor position at different load conditions are shown in Fig. 31.

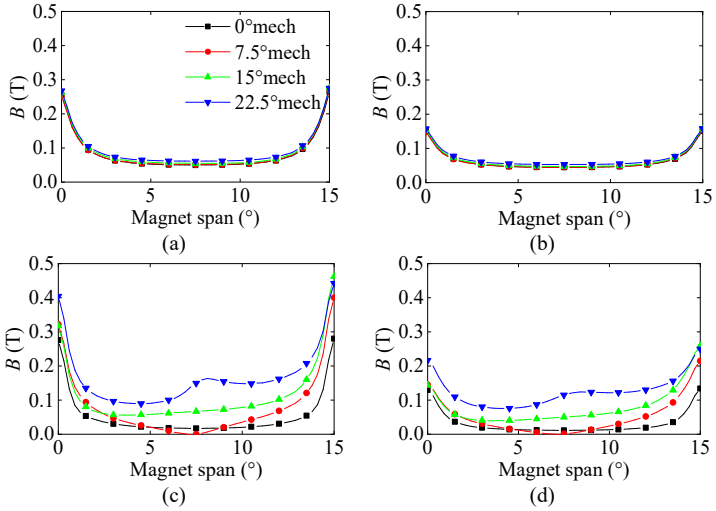

Fig. 30. Flux-density distributions over the magnet span of (a) the stator-installed rare-earth magnet, (b) the stator-installed ferrite magnet, (c) the rotor-installed rare-earth magnet, and (d) the rotor-installed ferrite magnet at various rotor positions.

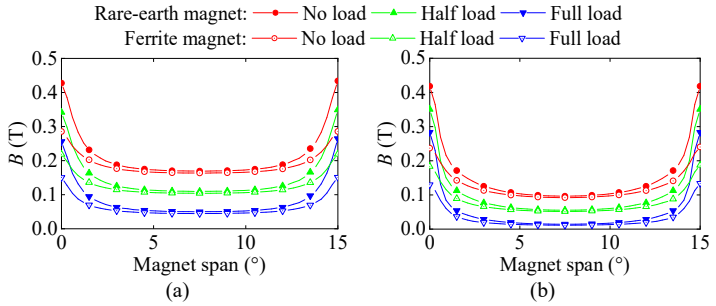

Fig. 31. Flux-density distributions over the magnet span of (a) the stator-installed magnet and (b) the rotor-installed magnet at various load conditions.

It is observed from Fig. 30 that the flux density in the stator-installed magnet is almost independent of the rotor position, while that in the rotor-installed magnet varies a lot. Fig. 31 indicates that the flux density decreases when the load increases, and the magnet's operating point at the full-load condition is close to 0 T. This means that when the load becomes heavier, the magnet' operating point will absolutely move into the third quadrant of the magnet demagnetization curve, increasing the possibility for irreversible demagnetization.

B. Magnet Demagnetization Constraint

As illustrated above, the magnet's operating point is close to the abscissa axis of the magnet demagnetization curve at full load, and can even move to the third quadrant at heavier loads. Besides, the magnet property is highly temperature sensitive. For both the rare-earth and ferrite magnets, the knee points of the magnet demagnetization curves locate in the third quadrant at the ambient temperature (25°C), as shown in Fig. 32. In this case, the magnets operate in the reversible demagnetization situation. As the magnet temperature rises, the knee point of the rare-earth magnet moves to the second quadrant, enhancing the probability of irreversible demagnetization. However, the knee point of the ferrite magnet continues to decline with the temperature rise, making it more tolerant of demagnetization. Apparently, the flux density at the knee point is a function of the magnet temperature, i.e. $B_D(T)$.

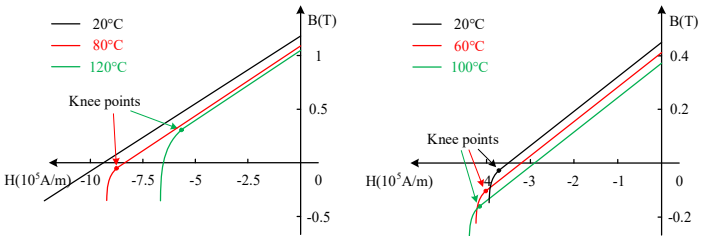

Fig. 32. Demagnetization curve of (a) the rare-earth magnet and (b) the ferrite magnet.

Based on the MEC model of the PM-shield ADS-SRM, the relationship between the maximum allowed current level i_m and the value of B_D is expressed as (9). Since the saturation of the iron core is negligible near unaligned rotor position, the iron-core reluctance is ignored in the MEC model. It should be noted that the value of B_D in the MEC computation is the flux density at the bulk of the magnet, neglecting the local demagnetization.

$$i_m(T) = \min\left[i_{m1}(T), i_{m2}(T), i_{m3}(T)\right] \tag{9}$$

In (9),

$$i_{m1}(T) = \frac{8F_{PM1}(T) - 4B_D(T)\tau_s\alpha_s R_o h_s R_{gopp}}{N_{ph}}$$

$$i_{m2}(T) = \frac{8F_{PM2}(T) - 4B_D(T)\tau_s\alpha_s R_i h_s R_{gipp}}{N_{ph}}$$

$$i_{m3}(T) = \frac{1}{N_{ph}}\left[8F_{PM3}(T) - \frac{4B_D(T)\tau_s\alpha_s\left(R_o^2 - R_i^2\right)R_{adj}R_{go}R_{gi}}{R_{adj}R_{gi} + R_{adj}R_{go} + 4R_{go}R_{gi}}\right]$$

where $F_{PM1}(T)$, $F_{PM2}(T)$, and $F_{PM3}(T)$ are the MMFs of the

magnet at temperature T.

The value of B_D and the corresponding maximum allowed current level i_m for the rare-earth and ferrite magnets in the PM-shield ADS-SRMs at various magnet temperatures are shown in Table III. It is indicated that the motor's maximum overload capability in safe operation is restricted by the magnet demagnetization behavior. For the rare-earth PM-shield ADS-SRM, the overload capability is significantly reduced at high temperatures, but it increases for the ferrite configuration. Their intersection is about 70°C. The rare-earth configuration allows 5.7 times higher overload capability than the ferrite configuration at 20°C, while it is only 40% at 80°C. This feature enables the two configurations suitable for different operation temperatures. For ensurance of the safe operation at 1.5 times the rated current, i.e. the current chopping level of 12A, the recommended operation temperature is below 73°C for the rare-earth configuration and above 47°C for the ferrite configuration. However, it is noted that, although the ferrite magnet is more tolerant of demagnetization at higher temperatures, the ferrite magnet should be absolutely demagnetized at heavy loads at low temperatures, which means that it can even be demagnetized during motor starting and speed regulation. This defect dismisses the ferrite PM shield from the most applications. Besides, as the operation temperature is generally high enough at heavy loads, the thermal analysis at the overload condition is much more important for the rare-earth configuration.

TABLE III
THE VALUE OF B_D AND MAXIMUM ALLOWED CURRENT LEVEL AT VARIOUS MAGNET TEMPERATURES

T (°C)	Rare-earth magnet		Ferrite magnet	
	B_D (T)	i_m (A)	B_D (T)	i_m (A)
20	-0.8	53.5	-0.02	9.4
60	-0.3	24.7	-0.09	13.3
80	-0.1	5.8	-0.12	15.3

C. Thermal Behavior

The results from the previous section suggest that the motor performance is tightly constrained by the magnet property as it is highly temperature sensitive. Besides, the overload capability is limited by the temperature rise in the winding insulation. In this study, the natural cooling method is employed. The temperature distributions in the machines are analyzed through the lumped parameter thermal network (LPTN) model. Fig. 33 shows the sectional drawing of the PM-shield ADS-SRM, and the corresponding general LPTN model of the rare-earth and ferrite PM-shield ADS-SRMs is given in Fig. 34. In Fig. 34, the blue dashed frames represent different motor parts, and the component subscripts are unique in each motor part. Based on the LPTN model, their thermal behaviors can be analyzed at various speeds and load conditions.

Table IV shows the steady-state temperatures in some critical parts of the original design and the rare-earth and ferrite PM-shield configurations at the rated condition. For a comparative study purpose, the experimental measurement is performed on the original design. Since three thermistors (KTY84-130) are buried in the outer portion, middle portion, and inner potion of the winding, only the measured results in these three parts are provided. The developed LPTN model is proved to have high accuracy on the temperature predictions. Furthermore, it is indicated in Table IV that, at the rated condition, the phase currents of the PM-shield configurations are lower than their maximum allowed values at the computed magnet temperatures, and the computed winding temperatures are far lower than their stability limit (130°C for B-class insulation). Besides, as the stator magnet and the middle portion of the winding exhibit relatively higher temperatures, the performance of the PM-shield configurations is mainly restricted by the thermal behavior of these two parts.

The transient magnet and middle-winding temperatures at full load at various speeds are shown in Fig. 35. As the central node of the equivalent thermal network provides the mean temperature of each motor part, the local temperature could be rather high. In order to avoid the excessive local temperature, the experimental measurement in the original design is performed until the measured temperature reaches 90°C. It is found that the measured results match well with the predictions. Besides, it is indicated in Fig. 35 that the safe operations of the rare-earth and ferrite PM-shield ADS-SRMs are limited by the stator-magnet and middle-winding temperatures, respectively. For either the rare-earth or ferrite configuration, the maximum allowed time for continuous operation extends with the rise of speed, e.g. 55 min at 200 r/min and 85 min at 500 r/min for the rare-earth configuration. When the rotor speed is high enough, the magnet and middle-winding temperatures will not exceed their stability limits. This is due to the enhanced heat convection in the air gap and at the exterior of the rotor at high speed.

As the thermal analysis at the overload condition is much more important for the rare-earth configuration, the transient magnet and winding temperatures at the overload conditions (1.5 times and twice the rated current) at 500 r/min are analyzed on this configuration. The computation results are shown in Fig. 36. It is indicated that the maximum allowed time for continuous operation is significantly shortened with the increase of the load. The continuous operation time should be no longer than 15 min and 6 min for operations at 1.5 times and twice the rated current, respectively.

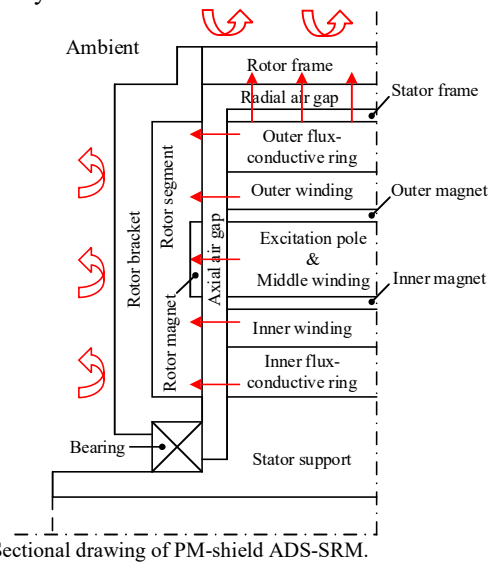

Fig. 33. Sectional drawing of PM-shield ADS-SRM.

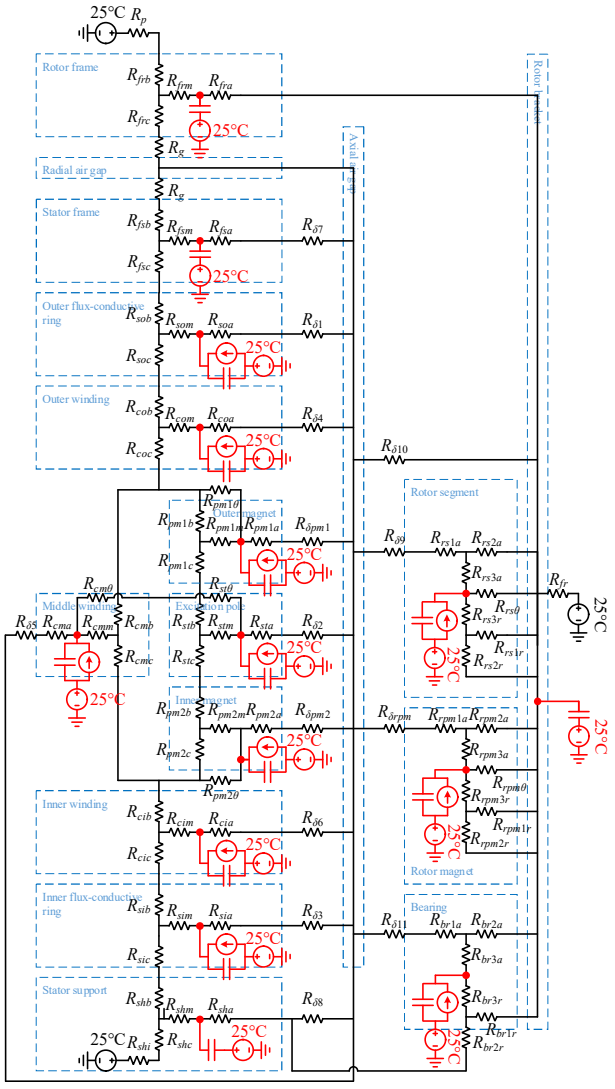

Fig. 34. General LPTN model of the rare-earth and ferrite PM-shield ADS-SRMs.

TABLE IV
STEADY-STATE TEMPERATURES (°C) AT THE RATED CONDITION

Motor parts		Original design		PM-shield configuration	
		LPTN	Exp.	Rare-earth	Ferrite
Excitation poles		64.8	-	58	52.4
Rotor segments		41.8	-	40.1	39.8
Windings	Outer portion	58.8	64.1	53.7	50.7
	Middle portion	65.1	66.3	57.8	51.9
	Inner portion	58.9	64.5	53.4	49.5
Stator magnets	Outer side	-	-	57.7	51.9
	Inner side	-	-	57.9	52.1
Rotor magnets		-	-	40	39.7

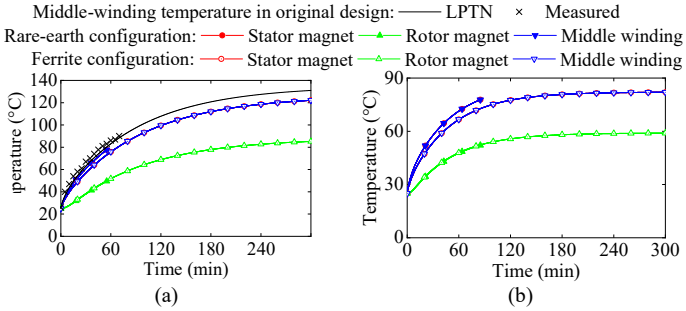

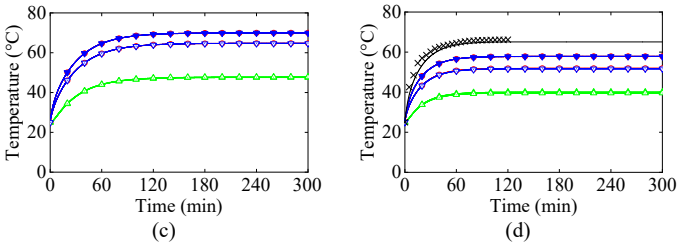

Fig. 35. Transient magnet and winding temperatures at full load at (a) 200 r/min, (b) 500 r/min, (c) 1000 r/min, and (d) 2000 r/min.

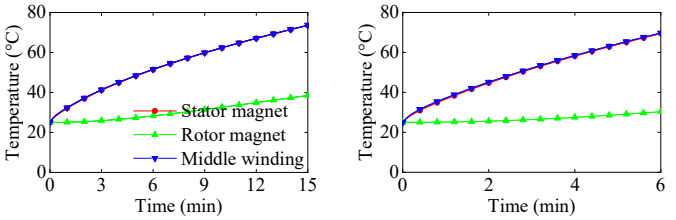

Fig. 36. Transient magnet and winding temperatures at (a) 1.5 times and (b) twice the rated current at 500 r/min.

VI. CONCLUSION

As presented in this paper, the PM-shield ADS-SRM has the feature to reduce the leakage field and weaken the magnetic saturation in the iron core. This is supported by the static magnetic analyses on the magnetic field distributions, flux linkages, phase inductances, and torque components. Besides, the motion-coupled analysis has been carried out to prove the significant improvement in the torque-production capability and efficiency. The results suggest that the rare-earth PM-shield configuration in Scheme #2 exhibits more superior performance than Scheme #1. Compared with the magnet-free topology, the average torque and efficiency of Scheme #2 are improved by about 21% and 3.2%, respectively, while the torque ripple coefficient decreases by about 11% at the rated condition.

Considering the cost reduction and the stable ferrite-magnet supply, an alternative proposal using ferrite magnets is applied to the PM-shield configuration. The performance of the ferrite PM-shield ADS-SRM is proved comparable to the rare-earth configuration. However, the magnet demagnetization analysis has demonstrated the defect of the ferrite PM shield that the ferrite magnet is ease of demagnetization even during motor starting and speed regulation, which dismisses the ferrite PM shield from the most applications.

As a whole, the PM shield shows promise for the performance improvement of electrical machines despite the more stringent operating conditions caused by the magnet demagnetization. Besides, the rare-earth magnet is still the first choice for the PM shield even though the ferrite magnet is low cost.

REFERENCES

[1] R. Krishnan, "Switched reluctance motor drives: modeling, simulation, analysis, design and applications," Boca Raton, FL: CRC Press, Jun. 2001.

[2] D. Lee, T. H. Pham and J. Ahn, "Design and operation characteristics of four-two pole high-speed SRM for torque ripple reduction," *IEEE Transactions on Industrial Electronics*, vol. 60, no. 9, pp. 3637-3643,

Sept. 2013.

[3] E. W. Fairall, B. Bilgin, and A. Emadi, "State-of-the-art high-speed switched reluctance machines," in *Proc. of IEEE International Electric Machines and Drives Conference*, Coeur d'Alene, ID, USA, pp. 1621-1627, may 2015.

[4] E. Bostanci, M. Moallem, A. Parsapour and B. Fahimi, "Opportunities and challenges of switched reluctance motor drives for electric propulsion: a comparative study," *IEEE Transactions on Transportation Electrification*, vol. 3, no. 1, pp. 58-75, Mar. 2017.

[5] C. Gan, J. Wu, Q. Sun, W. Kong, H. Li and Y. Hu, "A review on machine topologies and control techniques for low-noise switched reluctance motors in electric vehicle applications," *IEEE Access*, vol. 6, pp. 31430-31443, 2018.

[6] J. Lin, N. Schofield and A. Emadi, "External-rotor 6-10 switched reluctance motor for an electric bicycle," *IEEE Transactions on Transportation Electrification*, vol. 1, no. 4, pp. 348-356, Dec. 2015.

[7] B. Howey, B. Bilgin and A. Emadi, "Design of a mutually coupled external-rotor direct drive e-bike switched reluctance motor," *IET Electrical Systems in Transportation*, vol. 10, no. 1, pp. 89-95, 3 2020.

[8] S. Li, S. Zhang, T. G. Habetler and R. G. Harley, "Modeling, design optimization, and applications of switched reluctance machines—a review," *IEEE Transactions on Industry Applications*, vol. 55, no. 3, pp. 2660-2681, May-June 2019.

[9] R. Cao, E. Su and M. Lu, "Comparative study of permanent magnet assisted linear switched reluctance motor and linear flux switching permanent magnet motor for railway transportation," *IEEE Transactions on Applied Superconductivity*, vol. 30, no. 4, pp. 1-5, June 2020.

[10] I. Boldea, L. N. Tutelea, L. Parsa and D. Dorrell, "Automotive electric propulsion systems with reduced or no permanent magnets: an overview," *IEEE Transactions on Industrial Electronics*, vol. 61, no. 10, pp. 5696-5711, Oct. 2014.

[11] H. Torkaman, A. Ghaheri and A. Keyhani, "Axial flux switched reluctance machines: a comprehensive review of design and topologies," *IET Electric Power Applications*, vol. 13, no. 3, pp. 310-321, 3 2019.

[12] T. J. Woolmer and M. D. McCulloch, "Analysis of the yokeless and segmented armature machine," 2007 *IEEE International Electric Machines & Drives Conference*, Antalya, 2007, pp. 704-708.

[13] B. Bilgin, A. Emadi and M. Krishnamurthy, "Design considerations for switched reluctance machines with a higher number of rotor poles," *IEEE Transactions on Industrial Electronics*, vol. 59, no. 10, pp. 3745-3756, Oct. 2012.

[14] B. C. Mecrow, E. A. El-Kharashi, J. W. Finch and A. G. Jack, "Preliminary performance evaluation of switched reluctance motors with segmental rotors," *IEEE Transactions on Energy Conversion*, vol. 19, no. 4, pp. 679-686, Dec. 2004.

[15] Do Hyun Kang, "Increasing of thrust force in transverse flux machine by permanent-magnet screen," *IEEE Transactions on Magnetics*, vol. 41, no. 5, pp. 1952-1955, May 2005.

[16] R. Krishnan, "Permanent magnet synchronous and brushless DC motor drives," CRC Press/Taylor & Francis, 2010.

[17] Y. H. Jeong, D. H. Kang, J. M. Kim and S. M. Jang, "A design of transverse flux motor with permanent magnet shield," in *Proc. of ISIE 2001. 2001 IEEE International Symposium on Industrial Electronics Proceedings*, Pusan, South Korea, 2001, pp. 995-999 vol.2.

[18] W. Li and K. T. Chau, "Design and analysis of a novel linear transverse flux permanent magnet motor using HTS magnetic shielding," *IEEE Transactions on Applied Superconductivity*, vol. 20, no. 3, pp. 1106-1109, June 2010.

[19] A. Labak and N. C. Kar, "Designing and prototyping a novel five-phase pancake-shaped axial-flux SRM for electric vehicle application through dynamic FEA incorporating flux-tube modeling," *IEEE Transactions on Industry Applications*, vol. 49, no. 3, pp. 1276-1288, May-June 2013.

[20] A. Labak and N. C. Kar, "Novel approaches towards leakage flux reduction in axial flux switched reluctance machines," *IEEE Transactions on Magnetics*, vol. 49, no. 8, pp. 4738-4741, Aug. 2013.

[21] W. Sun, Q. Li, L. Sun and L. Li, "Development and investigation of novel axial-field dual-rotor segmented switched reluctance machine," *IEEE Transactions on Transportation Electrification*, 2020, doi: 10.1109/TTE.2020.3033668.

[22] J. A. Walker, D. G. Dorrell and C. Cossar, "Flux-linkage calculation in permanent-magnet motors using the frozen permeabilities method," *IEEE Transactions on Magnetics*, vol. 41, no. 10, pp. 3946-3948, Oct. 2005.

[23] G. J. Li, Z. Q. Zhu, X. Y. Ma and G. W. Jewell, "Comparative study of torque production in conventional and mutually coupled SRMs using frozen permeability," *IEEE Transactions on Magnetics*, vol. 52, no. 6, pp. 1-9, June 2016.

[24] D. G. Dorrell, M. Hsieh and A. M. Knight, "Alternative rotor designs for high performance brushless permanent magnet machines for hybrid electric vehicles," *IEEE Transactions on Magnetics*, vol. 48, no. 2, pp. 835-838, Feb. 2012.

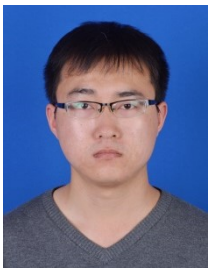

Wei Sun was born in Jiangsu Province, China. He received the B.S. degree in electrical engineering from Nanjing University of Science and Technology (NJUST), Nanjing, China, in 2014.

He is currently pursuing the Ph.D. degree in the School of Automation, NJUST, Nanjing, China. His main research interest focuses on electric motor design and control.

Qiang Li was born in Jiangsu Province, China. He received the B.S. degree from Harbin Institute of Technology (HIT), Harbin, China, in 1992, and the Ph.D. degree in electrical engineering from Southeast University, Nanjing, China, in 2005.

In 2005, he joined the Department of Electrical Engineering, School of Automation, Nanjing University of Science and Technology (NJUST), where he has been engaged in teaching and research in the field of electrical engineering. His main research interests include electric motor design, motor control, switching mode power supply, and embedded systems.

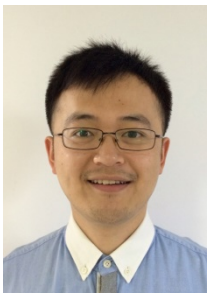

Le Sun (IEEE S'15–M'17) received the B.S. and M.S. degrees from Nanjing University of Aeronautics and Astronautics, Nanjing, China, in 2009 and 2012, respectively, and the Ph.D. degree in electrical engineering from the School of Electrical Engineering, Southeast University, Nanjing, China, in 2016.

He is now working as an associate professor in the department of electrical engineering, Nanjing University of Science and Technology (NJUST), Nanjing, China. From 2012 to 2013, he was a R&D Engineer with the United Automotive Electronic Systems Company, Ltd., Shanghai. From 2016 to 2018, he was working with the McMaster Automotive Resource Centre, McMaster University, where he was leading a research team of the motor control technologies. His research interest includes analysis, design, and control of permanent-magnet motors and power management techniques for electric vehicle (EV) and hybrid EV applications.

Xuefeng Jiang (S'15-M'17) received the B.S. degree in electrical engineering from Southwest Jiaotong University, Chengdu, China, in 2011, and the Ph.D. degrees in electrical engineering from Nanjing University of Aeronautics and Astronautics (NUAA), Nanjing, China, in 2017.

Since 2017, he has been with the Nanjing University of Science and Technology (NJUST), where he is currently an Assistant Professor with the Department of Electrical Engineering, School of Automation. He has authored or coauthored more than 20 technical papers. He is the holder of more than 20 issued patents. His teaching and research interest include design and control for electric machines, fault diagnosis, and fault-tolerant control for electric drive systems.